

Supplementary Materials

Mountains to climb: on the role of seamounts in upwelling of deep ocean waters through turbulent mixing

A. Mashayek¹, J. Gula^{2,3}, L. Baker⁴, A. Naveira Garabato⁵, L. Cimoli⁶, and J. Riley⁷

1,4 Imperial College London

²Univ Brest, CNRS, IRD, Ifremer, Laboratoire d'Océanographie Physique et Spatiale (LOPS), IUEM, Brest, France

³Institut Universitaire de France (IUF), Paris, France

⁵University of Southampton

⁶Scripps Institution of Oceanography

⁶University of Washington

2021

2021

Velocity data from the LLC4320 model

Average flow speeds at the mid-heights of seamounts in the KW11 census are calculated from the Estimating the Circulation and Climate of the Ocean (ECCO, <https://ecco-group.org>) Project's 1/48 MITgcm general circulation model (Rocha et al., 2016; Arbic et al., 2018), and processed using <https://pangeo.io/>. First, a daily mean of kinetic energy (KE) is found at each seamount by spatially averaging the KE over a disk of radius $a + 10\text{km}$ (where a is the seamount radius at half height from KW11) at the vertical level nearest to the seamount mid-height (again, inferred from the seamount height in KW11). This spatial mean is found every 3 hours, then averaged over the day to ‘de-tide’ the end result. The daily mean is found every 2 weeks, and then averaged over a year of the 14-month simulation. Finally, the average flow speed at each seamount is found as the square root of the mean KE.

The extracted velocity map is shown in Fig 1 herein and is employed in construction of Fig 1c in the main text, as well as in Figs 1 and 2 herein.

Equatorial Region Model

Figure 2 in the main text shows a dynamically downscaled regional simulation of the Equatorial Atlantic Ocean. The simulation is performed with the Coastal and Regional Ocean Community model (CROCO), which is built upon the Regional Oceanic Modelling System (ROMS, Shchepetkin and McWilliams, 2005). It solves the free surface, hydrostatic, and primitive equations using terrain-following vertical coordinates. The domain covers an area 900 km by 525 km (see Fig. 2c in the main text) with a grid-spacing of 750 m. It has 300 vertical levels in the vertical. The simulation is initialized and forced at its boundaries using the Atlantic-wide simulation GIGATL3 (Gula, 2021), which is a realistic simulation using the model CROCO with a grid spacing of 3-km and 100 vertical levels, covering the period 2004-2014. The simulation is run from February 2008 to September 2008. The time-mean variables are computed using the last 6 months of the simulation. The simulation is forced by hourly atmospheric forcings from the Climate Forecast System Reanalysis (CFSR, Saha et al., 2010), identical to GIGATL3 forcings. Tides are not included in this model solution. The bathymetry is taken from the SRTM30plus dataset Becker et al. (2009). The vertical mixing in the model is set by the K-profile parametrization (KPP, Large et al. (1994)) with a background diffusivity of $1 \times 10^{-5} \text{ m}^2 \text{ s}^{-1}$. There is no explicit lateral diffusivity in the simulation. The effect of bottom friction is parameterized through a logarithmic law of the wall with a roughness length $Z_0 = 0.01 \text{ m}$.

Drake Passage Model

Figure 3 in the main text shows a dynamically downscaled regional simulation of the Drake Passage at $\frac{1}{100}^{\circ}$ horizontal resolution performed using the MITgcm Marshall et al. (1997). The simulation covers an area of rough topography in the Drake Passage, and is nested within a larger patch Tulloch et al. (2014), which is itself

45 forced at the boundaries by restoring velocity, temperature and salinity to an ocean estimate that assimilated
46 a wide range of oceanographic in-situ and remote sensing data Forget (2010). The simulation closely mirrors
47 that described in Mashayek et al. (2017), with vertical resolution significantly improved to 225 (from 100)
48 vertical levels to resolve vertical structures and mixing. The vertical mixing in the model is set by the K-profile
49 parametrization (KPP, Large et al. (1994)) with a background diffusivity of $5 \times 10^{-5} \text{ m}^2 \text{ s}^{-1}$. Panel c shows
50 a comparison between the model's averaged diapycnal diffusivity with an averaged diffusivity inferred from
51 direct turbulence microstructure profiles taken within our simulation domain as a part of the Diapycnal and
52 Isopycnal Mixing Experiment in the Southern Ocean (DIMES) field experiment (see Mashayek et al. (2017)
53 for more details). The comparison is highly satisfactory. This model was shown to reproduce realistic density
54 stratification and mesoscale activity Tulloch et al. (2014) and to reproduce the advection and distribution of
55 the DIMES anthropogenically-injected tracer accurately Mashayek et al. (2017).

56 Gulf Stream Model

57 Figure 4 in the main text shows a dynamically downscaled regional simulation of the Gulf Stream. The simulation
58 is performed with the Coastal and Regional Ocean Community model (CROCO), which is built upon the
59 Regional Oceanic Modelling System (ROMS, Shchepetkin and McWilliams, 2005). It solves the free surface,
60 hydrostatic, and primitive equations using terrain-following vertical coordinates. The domain covers an area
61 1000 km by 800 km (see Fig. 4c in the main text) with a grid-spacing of 500 m. It has 256 vertical levels in
62 the vertical. Boundary conditions are supplied by a sequence of two lower resolution simulations that span the
63 entire Gulf Stream region and the Atlantic basin, respectively. The simulation is forced by daily winds and
64 diurnally modulated surface fluxes, as described in details in Gula et al. (2016). The 500-m simulation is run
65 from January to July. The time-mean variables are computed using the last 5 months of the simulation. Tides
66 are not included in this model solution. The bathymetry is taken from the SRTM30plus dataset Becker et al.
67 (2009). The vertical mixing in the model is set by the K-profile parametrization (KPP, Large et al. (1994)) with
68 a background diffusivity of $1 \times 10^{-5} \text{ m}^2 \text{ s}^{-1}$. There is no explicit lateral diffusivity in the simulation. The effect
69 of bottom friction is parameterized through a logarithmic law of the wall with a roughness length $Z_0 = 0.01$
70 m. This simulation is identical to the one used in Klymak et al. (2016), except for the vertical resolution (256
71 levels instead of 50 levels).

72 Construction of the global diffusivity map

73 To construct a mixing map based on the layered seamount wave vortices, we filtered the KW11 data and left
74 out seamounts (a) that generate barotropic vortices and Taylor Columns ($Bu < 1$; even though such vortices
75 can induce interesting dynamics such as lee waves see Fig. 1d in the main text), (b) that are in close vicinity of
76 the equator at which $Ro > 1$ and the scaling relations Eq. 1 in the main text fails to hold (see the global map
77 of seamount Ro in Fig 2 herein), (c) at which the flow is primarily expected to go above and not around them
78 (see the map of Fr in Fig 1c in the main text), and (d) that are shorter than 100 m and likely are entrained in
79 boundary layer turbulence. Eq. (1) from the main text was applied to the surviving KW11 seamounts to infer
80 diffusivities (see Fig 5a in the main text). Note that we used a proportionality factor of 3 in Eq. (1) based on
81 Fig 11 of Perfect et al. (2020).

82 To construct a continuous map of seamount mixing to be used in global watermass transformation calcula-
83 tions, we use the distribution of diffusivity for the seamounts which survive the above-mentioned filtering
84 (shown in Fig 5a of the main text) to construct a 2D ‘map’ of mixing on the seafloor on a $1/2^\circ$ (approximately
85 50km) latitude-longitude grid. For each 2D cell, the total mixing is calculated as the sum of that due to all
86 the qualifying seamounts within the cell. This is justified since having even one seamount within a 50km grid
87 cell fills out its volume since (I) almost all the qualifying seamounts have a diameter larger than 10km (with
88 most larger than 20km), and (II) Eq. 1 in the main text represents a diffusivity averaged over a volume of one
89 diameter around each seamount. This methodology is conservative as (a) it does not account for more complex
90 wake dynamics in between neighbouring seamounts which lead to enhanced diffusivity as shown by the realistic
91 examples in the main text and (b) does not account for the contribution of seamounts to mixing within the
92 neighbouring cells (i.e. each seamount only contributes to the cell within which its centre is located). As with
93 all other choices in our work, we leaned on a more conservative estimate and avoided any interpolation to avoid
94 generation of spurious mixing. The mean height of the qualifying seamounts within a cell is also calculated.
95 The 2D map is then translated into a 3D map on the same grid as the WOCE climatological hydrographic data:
96 the total mixing in each basal 2D grid cell is projected upward using a tanh profile which is 1 from the seafloor
97 to a height above the bottom equal to the mean seamount height within the cell, and is zero above that.

98 Finally, we note that we do not explicitly account for influence of tides on the wake vortices, based on the
99 argument that for the most part it is minor. To assess this, we calculated the tidal excursion (see Fig 4 herein),
100 the ratio of the distance travelled by a water parcel due to the M2 tide to the seamount diameter and found the
101 ratio at the KW11 seamounts to be generally much less than one, indicating that the scale of the seamounts is

such that tidal flow is likely secondary to the mean flow for the generation of wake vortices. While this is true in a global sense, however, turbulence generated by tidal flow around seamounts through internal tides or other processes may be important in enhancing mixing Kunze and Toole (1997); Puthan et al. (2021), furthering the conservatism in our mixing estimates.

Diapycnal mixing estimates

Internal wave-driven turbulence can lead to the irreversible transformation of water masses, which may become either lighter or denser. The sign and the rate of the water mass transformation depend on the diapycnal divergence of the buoyancy flux: water masses are transformed only if mixing is vertically non-homogeneous, i.e. if there is a diffusive convergence or divergence of water masses. Water moves across density surfaces at the diapycnal velocity:

$$\mathbf{e} = \frac{\partial_{\mathbf{z}} \mathcal{M}}{\partial_{\mathbf{z}} \mathbf{b}}. \quad (1)$$

where $b = -(g/\rho_0)\delta\rho$ is the buoyancy and \mathcal{M} is the buoyancy flux.

The diapycnal velocity is positive and waters become lighter when the buoyancy flux arising due to mixing (\mathcal{M}) decreases with depth, for example when there is surface-intensified mixing, or in the bottom boundary layer where $\mathcal{M} \rightarrow 0$ towards the ocean floor (De Lavergne et al., 2016; Ferrari et al., 2016). Conversely, the diapycnal velocity is negative and waters become denser when mixing increases with depth, for example in the ocean interior near rough topography, where mixing is enhanced toward the bottom (De Lavergne et al., 2016; Ferrari et al., 2016; McDougall and Ferrari, 2017).

As an example, the diapycnal velocity associated with the estimates of internal tide- and lee wave-driven diapycnal mixing on the density surface $\gamma^n = 28.0.5$ is shown in Fig 5 herein (with the Pacific sector highlighted in Fig 5e in the main text): diapycnal upwelling (red) is occurring in proximity to rough topography, as well as over topographically smooth regions (e.g. North Pacific); conversely, diapycnal downwelling (blue) takes place in most of the ocean interior, and in particular around regions of underlying rough topography.

The water mass transformation rate across a neutral density surface γ_*^n in the ocean interior is given by the integral of the diapycnal velocity over that density surface:

$$\mathcal{D}(\gamma_*^n) = - \iint_{A(\gamma_*^n)} \tilde{\mathbf{e}} \cdot \hat{\mathbf{n}} dA \quad (2)$$

where $\hat{\mathbf{n}}$ is the unit vector normal to the density surface, A is the surface area of the density surface, and the minus sign is used such that water mass transformation is positive when water goes from denser to lighter (following Ferrari et al. 2016). The water mass transformation is measured in Sverdrups. The net transformation rate is given by the residual of diapycnal upwelling (along the boundaries and in regions of vertically decaying buoyancy flux) and diapycnal downwelling (in the ocean interior, in particular in regions of vertically increasing buoyancy flux over rough topography).

Impact of the vertical mixing scheme

Sensitivity to the choice of the vertical mixing scheme and some parameters values has been evaluated by comparing results for the Gulf Stream Model with 3 different setups:

1. the K-profile parametrization (KPP, Large et al. (1994)) with a background diffusivity of $1 \times 10^{-5} \text{ m}^2 \text{ s}^{-1}$
2. The $k-\epsilon$ turbulence closure scheme with the Canuto A stability function formulation Umlauf and Burchard (2003); Canuto et al. (2001) using default ROMS parameters values (in particular $tke_{min} = 10^{-6} \text{ m}^2 \text{ s}^{-2}$), (Warner et al., 2005).
3. The $k - \epsilon$ turbulence closure scheme with reduced $tke_{min} = 10^{-10} \text{ m}^2 \text{ s}^{-2}$, as in Perfect et al. (2020).

The mean vertical profiles of diffusivity (Fig. 4d in the main text) are shown in Fig. 6 for the 3 configurations. All cases lead to the same qualitative behaviour, with a diffusivity in the seamount wake one or two orders of magnitude larger than the typical values at the same depth away from the seamount.

Comparison between diffusivities from scalings and from realistic simulations

A visualization of seamounts actually included in the database, versus the ones represented in the simulations' topography, is visible herein in Figures 7 and 8. In the Gulf Stream region, all visible seamounts are included in the database. However, in the equatorial region, some of the tallest seamounts (almost islands) are not included in the database because they are too close to the coast. These structures are also important sources of topographic interactions, and their absence is pointing to a conservative estimate of mixing due to seamounts

142 in this paper.

143
144 For all referenced seamounts, however, a comparison of diffusivity scalings with actual simulations' dif-
145 fusivities (averaged around the seamounts following the methodology used for the global estimation) points
146 systematically to a similar or lower order of magnitude for the scalings compared to the modelled diffusivities
147 around seamounts (Figures 7 and 8 herein). In the Gulf Stream region in particular, where most seamounts
148 correspond to a low- Bu regimes, scalings do not predict diffusivities as strong as in the model. This points
149 again toward an underestimation of the scalings compared to the model's diffusivities, which is explained by
150 the fact that other sources of diffusivities are included in the model (*e.g.*, internal waves), but more generally
151 confirms that scalings do not overestimate diffusivities, even in high- Ro realistic regimes such as the equatorial
152 one.

153
154 A final comparison is shown for simulations at different resolution: a high-resolution one ($\delta x = 500$ m /
155 256 lev) versus a moderate resolution ($\delta x = 3$ km / 100 lev) using the same model (and forcings) in Figure
156 8. The latter is unable to resolve the generation of vorticity and the vertical shears appearing in the wake of
157 the seamounts. The same is true for the Gulf Stream region (not shown). This highlights that models would
158 require a significant increase in horizontal and vertical resolution to be able to resolve such processes and the
159 associated diffusivities on a global scale.

160 References

- 161 Arbic, B. K., Alford, M. H., Ansong, J. K., Buijsman, M. C., Ciotti, R. B., Farrar, J. T., Hallberg, R. W.,
162 Henze, C. E., Hill, C. N., Luecke, C. A., et al. (2018). Primer on global internal tide and internal gravity wave
163 continuum modeling in HYCOM and MITgcm. *New frontiers in operational oceanography*, pages 307–392.
- 164 Becker, J. J., Sandwell, D. T., Smith, W. H. F., Braud, J., Binder, B., Depner, J., Fabre, D., Factor, J.,
165 Ingalls, S., Kim, S.-H., Ladner, R., Marks, K., Nelson, S., Pharaoh, A., Trimmer, R., Rosenberg, J. V.,
166 Wallace, G., and Weatherall, P. (2009). Global Bathymetry and Elevation Data at 30 Arc Seconds Resolution:
167 SRTM30_PLUS. *Mar. Geod.*, 32(4):355–371.
- 168 Canuto, V. M., Howard, A., Cheng, Y., and Dubovikov, M. (2001). Ocean turbulence. part i: One-point closure
169 model—momentum and heat vertical diffusivities. *Journal of Physical Oceanography*, 31(6):1413–1426.
- 170 De Lavergne, C., Madec, G., Le Sommer, J., Nurser, A. G., and Naveira Garabato, A. C. (2016). On the
171 consumption of antarctic bottom water in the abyssal ocean. *Journal of Physical Oceanography*, 46(2):635–
172 661.
- 173 Ferrari, R., Mashayek, A., McDougall, T. J., Nikurashin, M., and Campin, J.-M. (2016). Turning ocean mixing
174 upside down. *Journal of Physical Oceanography*, 46(7):2239–2261.
- 175 Forget, G. (2010). Mapping ocean observations in a dynamical framework: A 2004-06 ocean atlas. *Journal of
176 Physical Oceanography*, 40(6):1201–1221.
- 177 Gula, J. (2021). Mesharou/GIGATL: Description of the GIGATL simulations.
- 178 Gula, J., Molemaker, M., and McWilliams, J. C. (2016). Submesoscale dynamics of a Gulf Stream frontal eddy
179 in the South Atlantic Bight. *J. Phys. Oceanogr.*, 46:305–325.
- 180 Klymak, J., Shearman, R., Gula, J., Lee, C., D'Asaro, E., Thomas, L., Harcourt, R., Shcherbina, A., Sunder-
181 meyer, M., Molemaker, M., and McWilliams, J. C. (2016). Submesoscale streamers exchange water on the
182 North Wall of the Gulf Stream. *Geophys. Res. Lett.*, 43:1226–1233.
- 183 Kunze, E. and Toole, J. M. (1997). Tidally driven vorticity, diurnal shear, and turbulence atop fieberling
184 seamount. *Journal of Physical Oceanography*, 27(12):2663–2693.
- 185 Large, W. G., McWilliams, J. C., and Doney, S. C. (1994). Oceanic vertical mixing: A review and a model with
186 a nonlocal boundary layer parameterization. *Reviews of geophysics*, 32(4):363–403.
- 187 Marshall, J., Adcroft, A., Hill, C., Perelman, L., and Heisey, C. (1997). A finite-volume, incompressible navier
188 stokes model for, studies of the ocean on parallel computers. *J. Geophys. Res.*, 102(C3):5753–5766.
- 189 Mashayek, A., Ferrari, R., Merrifield, S., Ledwell, J. R., St Laurent, L., and Garabato, A. N. (2017). Topographic
190 enhancement of vertical turbulent mixing in the Southern Ocean. *Nature communications*, 8:14197.

- 191 McDougall, T. and Ferrari, R. (2017). Abyssal upwelling and downwelling driven by near-boundary mixing. *J.
192 Phys. Oceanogr.*, 47:261–283.
- 193 Perfect, B., Kumar, N., and Riley, J. J. (2020). Energetics of seamount wakes. part i: Energy exchange. *Journal
194 of Physical Oceanography*, 50(5):1365–1382.
- 195 Puthan, P., Sarkar, S., and Pawlak, G. (2021). Tidal synchronization of lee vortices in geophysical wakes.
196 *Geophysical Research Letters*, 48(4):e2020GL090905.
- 197 Rocha, C. B., Chereskin, T. K., Gille, S. T., and Menemenlis, D. (2016). Mesoscale to submesoscale wavenumber
198 spectra in drake passage. *Journal of Physical Oceanography*, 46(2):601–620.
- 199 Saha, S., Moorthi, S., Pan, H.-L., Wu, X., Wang, J., Nadiga, S., Tripp, P., Kistler, R., Woollen, J., Behringer,
200 D., et al. (2010). The ncep climate forecast system reanalysis. *Bulletin of the American Meteorological Society*,
201 91(8):1015–1058.
- 202 Shchepetkin, A. and McWilliams, J. C. (2005). The Regional Oceanic Modeling System (ROMS): A split-
203 explicit, free-surface, topography-following- coordinate ocean model. *Ocean Modelling*, 9:347–404.
- 204 Tulloch, R., Ferrari, R., and others (2014). Direct estimate of lateral eddy diffusivity upstream of Drake Passage.
205 *Journal of Physical Oceanography*, 44(10):2593–2616.
- 206 Umlauf, L. and Burchard, H. (2003). A generic length-scale equation for geophysical turbulence models. *Journal
207 of Marine Research*, 61(2):235–265.
- 208 Warner, J. C., Sherwood, C. R., Arango, H. G., and Signell, R. P. (2005). Performance of four turbulence
209 closure models implemented using a generic length scale method. *Ocean Modelling*, 8(1):81 – 113.

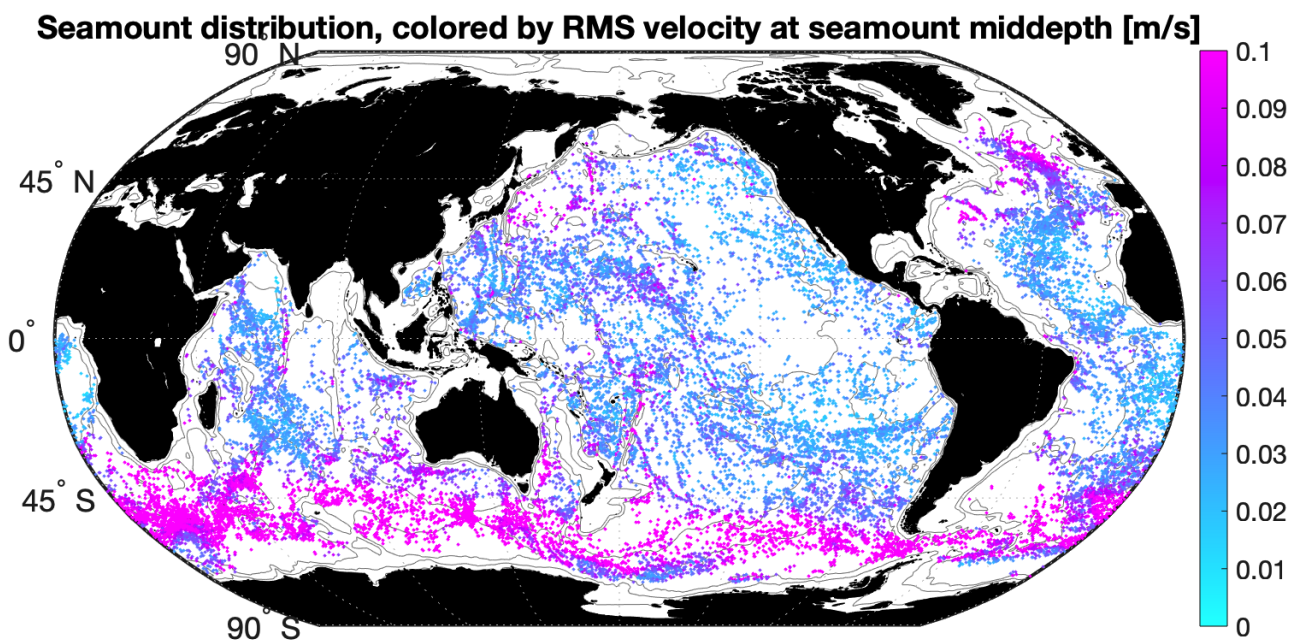


Figure 1: Similar to panels b,c in Fig 1 in the main text, but coloured by the root-mean-square velocity measured at seamount mid-depths. The velocity data are from Rocha et al. (2016); Arbic et al. (2018)

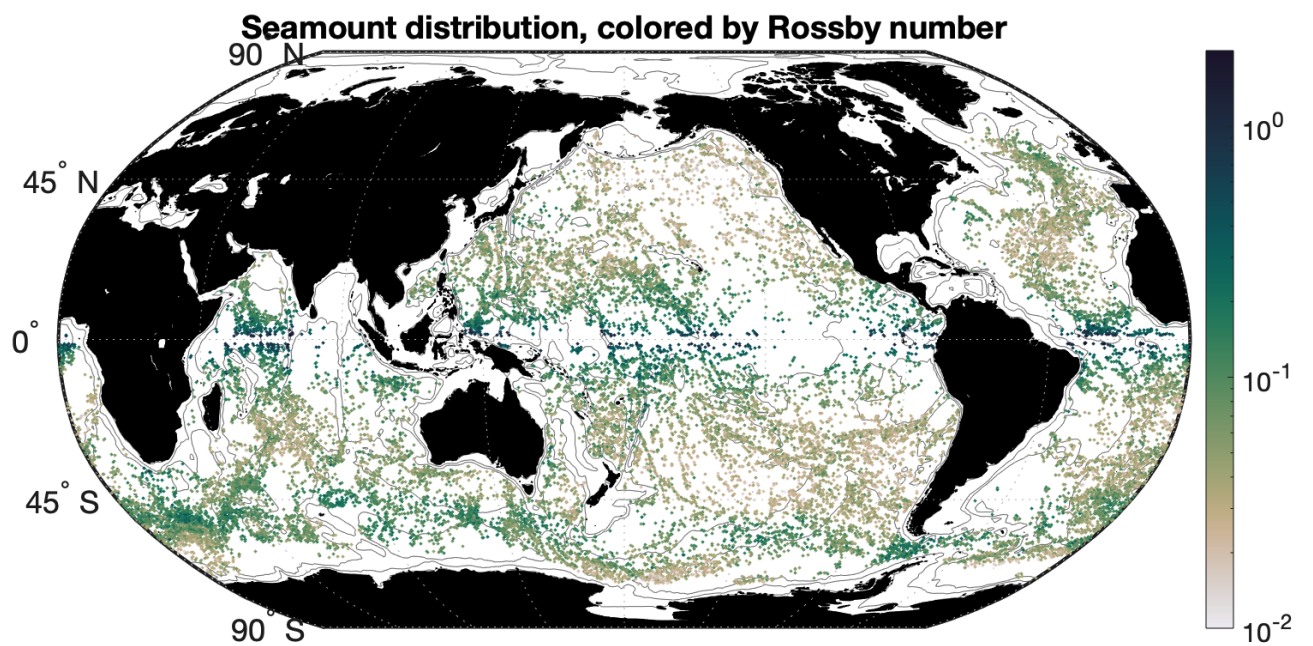


Figure 2: Similar to panels b,c in Fig 1 in the main text, but coloured with the seamount Rossby number.

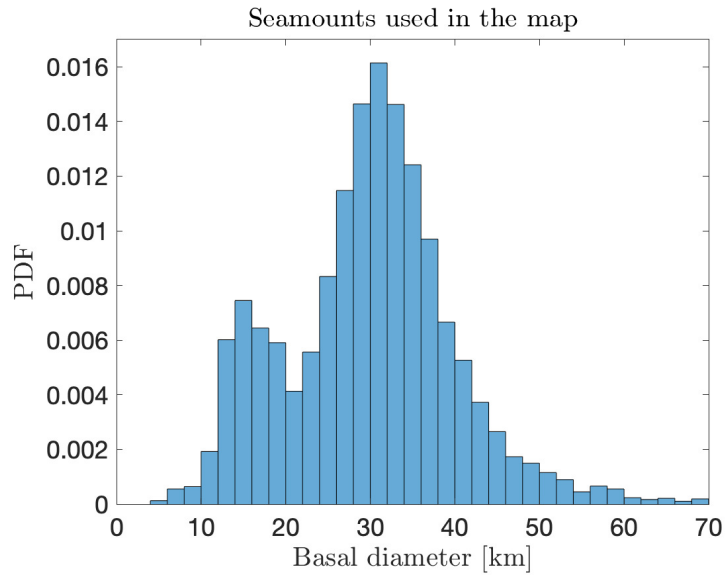


Figure 3: Basal diameter for the seamounts used in water mass transformation calculations (i.e. those in Fig 5a of the main text).

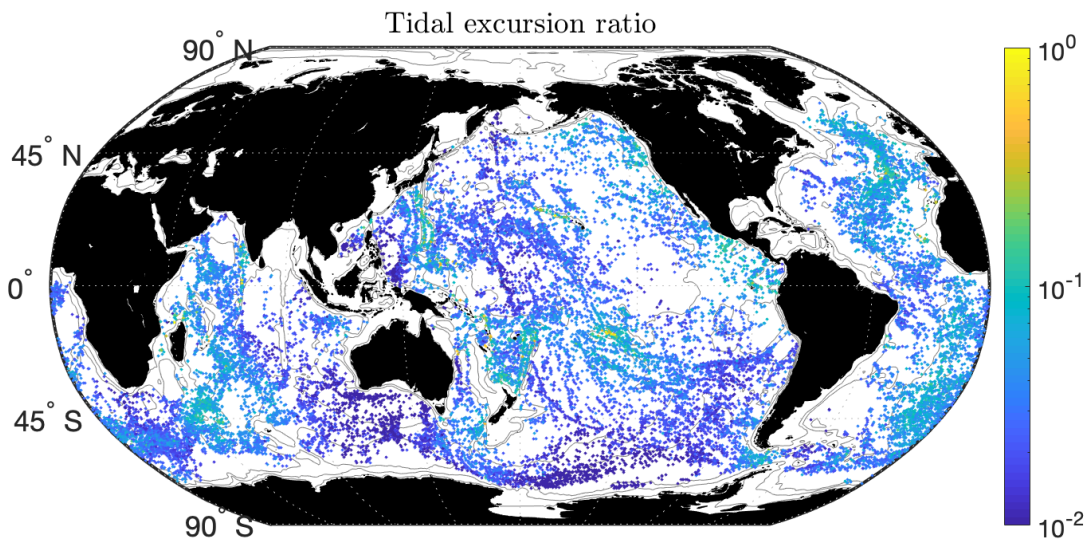


Figure 4: Tidal excursion ratio r at seamounts, calculated as $r = U_{M2}T/D$, where U_{M2} is the M2 component of the tidal speed from the TPXO9 tidal atlas (Egbert and Erofeeva 2002), T is half the semi-diurnal tidal period (= 6.25 h), and D is the seamount mid-height diameter.

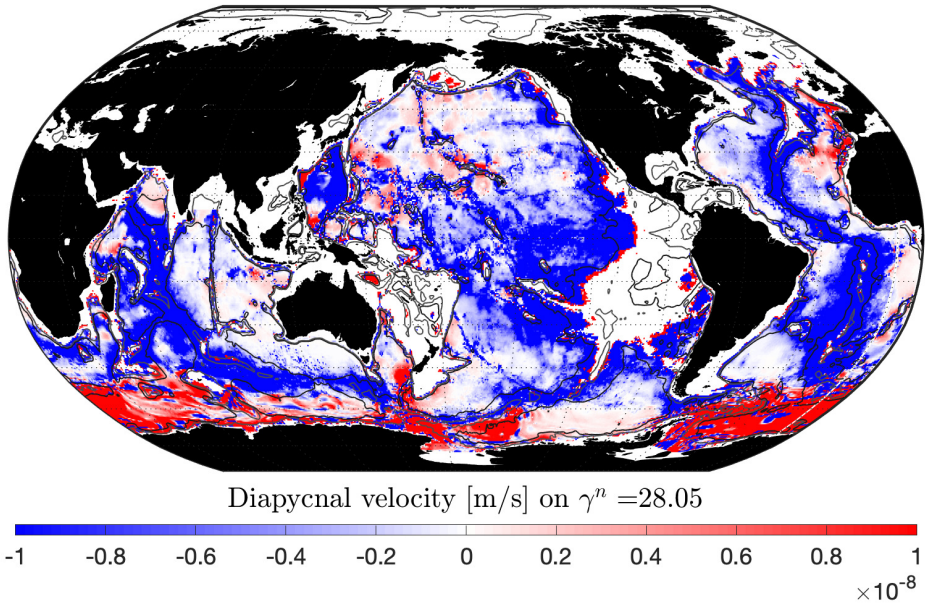


Figure 5: Diapycnal velocity on neutral density $\gamma^n = 28.05$ from the contribution of internal tides and lee waves. Positive values (red) indicate diapycnal upwelling, negative values (blue) indicate diapycnal downwelling.

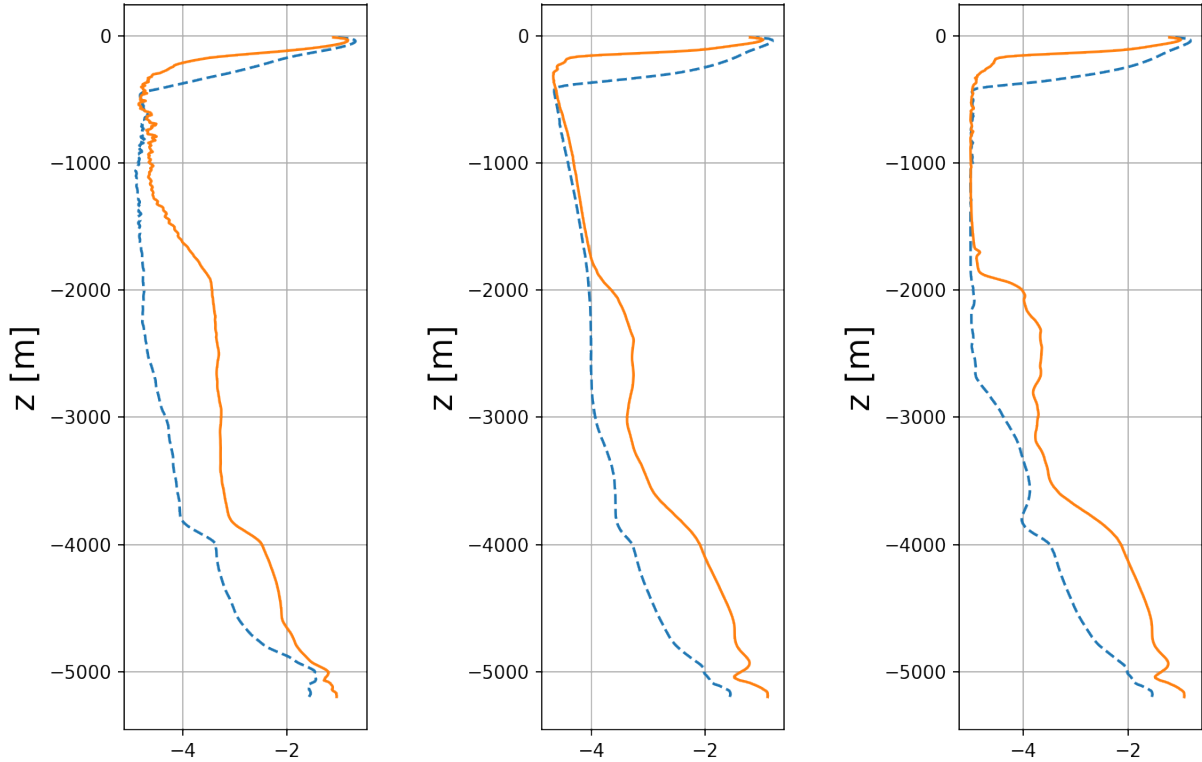


Figure 6: Time-mean vertical profiles of $\log_{10}(K_\rho)$, spatially integrated over the seamount wake region in solid orange lines (within the green box in Fig. 4f), and over the full domain in dashed blue line. (a) Simulation using KPP, (b) simulation using the $k - \epsilon$ turbulence closure scheme with $tke_{min} = 10^{-6} \text{ m}^2 \text{s}^{-2}$, and (c) simulation using the $k - \epsilon$ turbulence closure scheme with $tke_{min} = 10^{-10} \text{ m}^2 \text{s}^{-2}$.

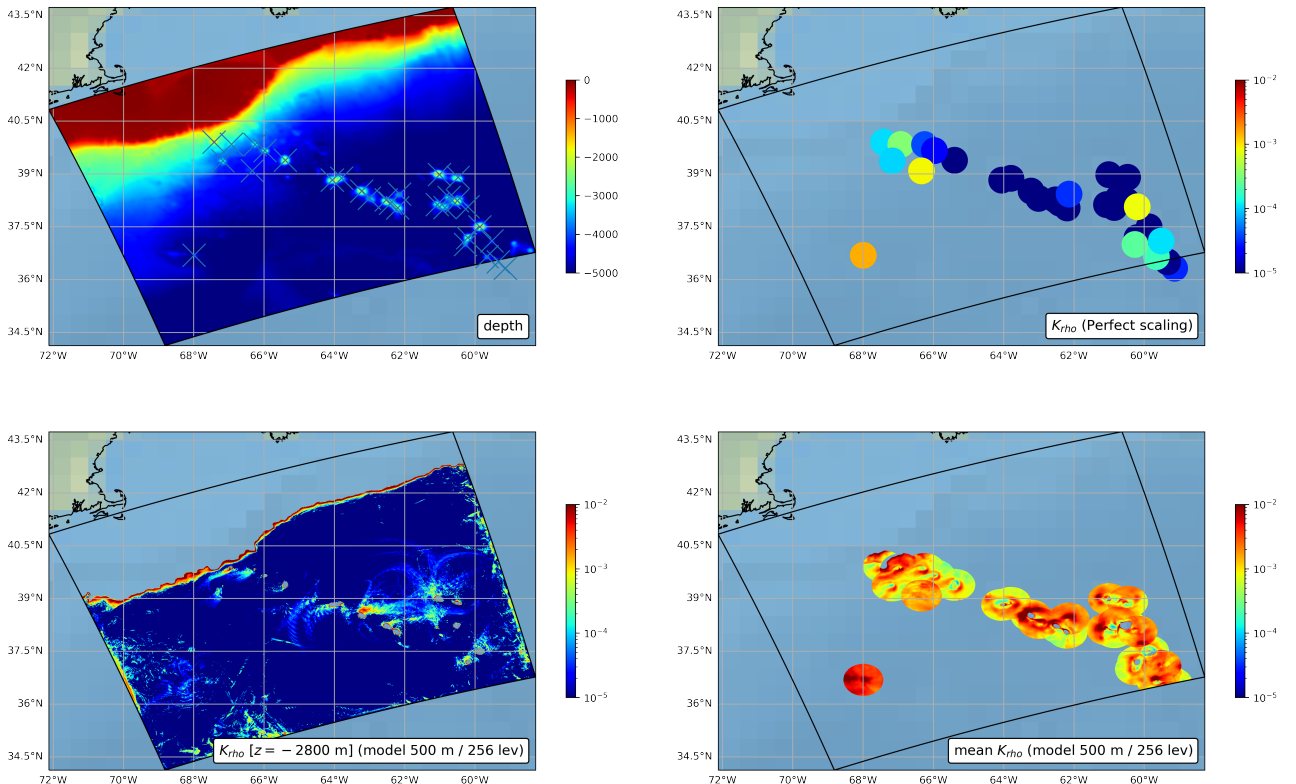


Figure 7: (a) Model topography with seamounts included in the database plotted as crosses. (b) Diffusivity scalings based on the seamount database. (c-d) Diffusivities from the simulation (c) along an horizontal section at 2800 m, and (d) volume averaged between the bottom and the top of the seamount.

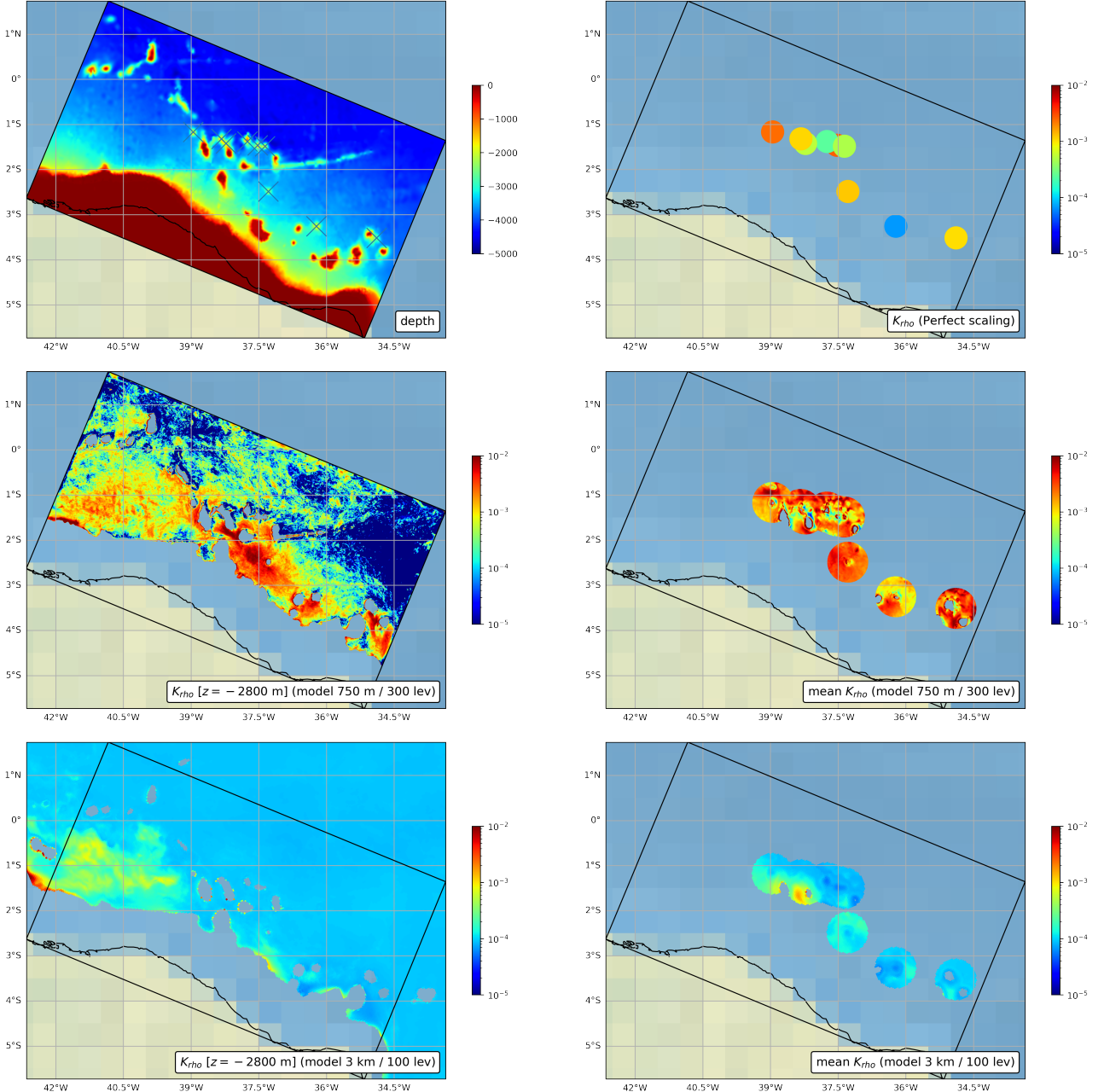


Figure 8: (a) Model topography with seamounts included in the database plotted as crosses. (b) Diffusivity scalings based on the seamount database. (c-d) Diffusivities from the high resolution simulation (c) along an horizontal section at 2800 m, and (d) volume averaged between the bottom and the top of the seamount. (e-f) Diffusivities from the GIGATL3 simulation (e) along an horizontal section at 2800 m, and (f) volume averaged between the bottom and the top of the seamount.